nature chemistry

ARTICLES

https://doi.org/10.1038/s41557-021-00737-8

Check for updates

Isolation of a triplet benzene dianion

Colin A. Gould[1], Jonathan Marbey[2,3], Veacheslav Vieru[4,8], David A. Marchiori[5], R. David Britt[5], Liviu F. Chibotaru[4], Stephen Hill[2,3] and Jeffrey R. Long[1,6,7] ✉

Baird's rule predicts that molecules with 4*n* π electrons should be aromatic in the triplet state, but the realization of simple ring systems with such an electronic ground state has been stymied by these molecules' tendency to distort into structures bearing a large singlet–triplet gap. Here, we show that the elusive benzene diradical dianion can be stabilized through creation of a binucleating ligand that enforces a tightly constrained inverse sandwich structure and direct magnetic exchange coupling. Specifically, we report the compounds $[K(18\text{-crown-6})(THF)_2]_2[M_2(BzN_6\text{-Mes})]$ (M = Y, Gd; BzN_6-Mes = 1,3,5-tris[2′,6′-(*N*-mesityl)dimethanamino-4′-*tert*-butylphenyl]benzene), which feature a trigonal ligand that binds one trivalent metal ion on each face of a central benzene dianion. Antiferromagnetic exchange in the Gd^{3+} compound preferentially stabilizes the triplet state such that it becomes the molecular ground state. Single-crystal X-ray diffraction data and nucleus-independent chemical shift calculations support aromaticity, in agreement with Baird's rule.

Aromaticity is a fundamental chemistry principle with broad utility, offering insights into molecular geometry, electronic structure and chemical reactivity[1,2]. Applications of aromaticity are diverse and range from the prediction of pericyclic reactions to the design of singlet-fission materials;[3,4] as such, a significant body of research has focused on developing a deeper understanding of this property[1,2,5]. Hückel's rule was the first formalism developed for aromaticity, predicting that cyclic, planar π systems in the ground singlet ($S = 0$) state are stabilized (aromatic) when they possess $4n + 2$ electrons and destabilized (antiaromatic) when they possess $4n$ electrons[6,7]. Subsequently, theories have been developed to describe more exotic cases: π systems with a half-twist can display Möbius aromaticity and molecules in the first excited triplet ($S = 1$) state can exhibit Baird aromaticity, both reversals of Hückel's rule in which $4n$ π electrons give rise to aromaticity[8–11].

Baird aromaticity is an excited-state property for most annulenes and is therefore quite challenging to study experimentally[12,13]. As a result, current understanding of this property is primarily based on analyses of photochemical reactivity, spectroscopy of photoexcited molecules and computational studies[14–21]. Ground-state Baird aromaticity was recently reported for a three-dimensionally conjugated macrocycle[22] and bicyclic Baird-type aromaticity—wherein two π systems that each possess $4n + 1$ electrons couple to form a triplet state that displays global aromaticity—was observed for a dithienothiophene-bridged [34]octaphyrin[23,24]. However, ground-state Baird aromaticity has remained elusive in monocyclic hydrocarbons[12,13], the canonical molecules for which the concept of aromaticity was first developed[1,2]. This is due to large energetic separation between the ground singlet and triplet excited states in monocyclic π systems with $4n$ electrons, caused by pseudo Jahn–Teller distortion[1,2,25]. For instance, cyclobutadiene derivatives adopt a rectangular structure and benzene dianions adopt a quinoidal or non-planar conformation, geometries that possess a well-isolated singlet ground state and a high-energy triplet excited state[1,2,25]. Indeed, the only known annulenes that possess a triplet ground state are certain cyclopentadienyl cations or benzene dications. However, these transient species were only characterized using electron paramagnetic resonance (EPR) spectroscopy after being trapped at low temperature[26,27]. Thus, the synthesis, isolation and characterization of a kinetically persistent monocyclic π system with a well-separated Baird-aromatic ground state represents an important and unsolved chemical challenge.

In this Article, we report the synthesis and characterization of trigonally symmetric inverse sandwich complexes $[M_2(BzN_6\text{-Mes})]^{2-}$ (M = Y, Gd; BzN_6-Mes = 1,3,5-tris[2′,6′-(*N*-mesityl)dimethanamino-4′-*tert*-butylphenyl]benzene), featuring two rare earth metal(III) ions bridged by a benzene dianion (Fig. 1). The rigid, trigonal scaffold preferentially stabilizes the D_{6h}-symmetric triplet state of the dianion relative to the C_{2v}- or D_{2h}-symmetric singlet state, leading to a singlet–triplet gap for the diamagnetic Y^{3+} congener that is orders of magnitude smaller than values typically observed for an annulene with $4n$ π electrons. Significantly, incorporation of paramagnetic Gd^{3+} facilitates strong magnetic exchange coupling, affording even greater stabilization to the triplet state such that it becomes the molecular ground state, enabling complete characterization of its aromaticity.

Results and discussion

Synthesis and structural characterization. The synthesis of the new binucleating ligand H_6BzN_6-R is highly modular and its steric bulk can be tuned by varying the R group of the aniline in the penultimate step (Supplementary Fig. 1). In our hands, metallation and subsequent reduction reactions with H_6BzN_6-4-*tert*-butylphenyl did not yield isolable dianion complexes (Supplementary Fig. 12), but use of H_6BzN_6-Mes (Mes = 2,4,6-trimethylphenyl) enabled isolation of the benzene monoanion- and benzene dianion-bridged compounds $[K(18\text{-crown-6})(THF)_2]_n[M_2(BzN_6\text{-Mes})]$ (M = Y, Gd; $n = 1$ (**1**), 2 (**2**)) as polycrystalline solids. Significantly, all compounds are indefinitely stable in the solid state at −30 °C under a nitrogen atmosphere. When dissolved in THF, the half-lives of **2-Y** and **2-Gd** are 10.1 and 26.5 h at 25 °C, respectively (Supplementary Figs. 19–22). This kinetic stabilization can be attributed to steric

[1]Department of Chemistry, University of California, Berkeley, CA, USA. [2]National High Magnetic Field Laboratory, Florida State University, Tallahassee, FL, USA. [3]Department of Physics, Florida State University, Tallahassee, FL, USA. [4]Theory of Nanomaterials Group, Katholieke Universiteit Leuven, Leuven, Belgium. [5]Department of Chemistry, University of California, Davis, CA, USA. [6]Department of Chemical and Biomolecular Engineering, University of California, Berkeley, CA, USA. [7]Materials Sciences Division, Lawrence Berkeley National Laboratory, Berkeley, CA, USA. [8]Present address: Maastricht Science Programme, Faculty of Science and Engineering, Maastricht University, Maastricht, The Netherlands. ✉e-mail: jrlong@berkeley.edu

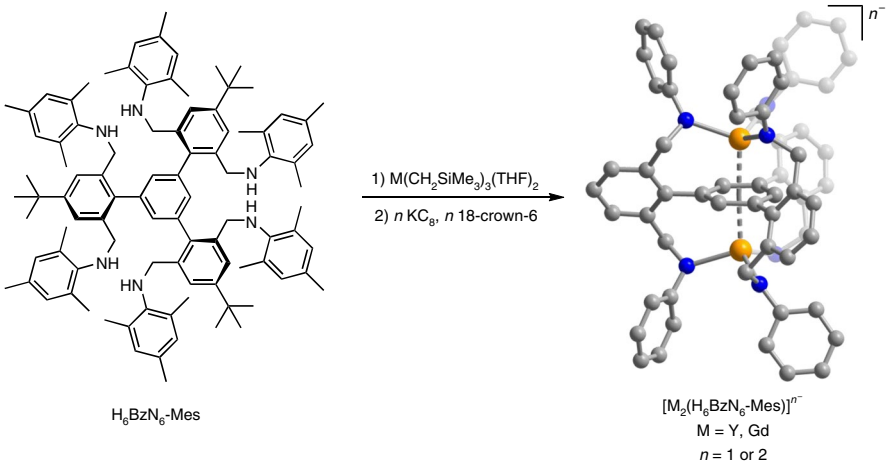

Fig. 1 | Synthesis and structure of $[M_2(BzN_6\text{-Mes})]^{n-}$ complexes. Synthesis of the four dinuclear compounds $[K(18\text{-crown-6})(THF)_2]_n[M_2(BzN_6\text{-Mes})]$ (M = Y, Gd; $n = 1$ (**1-Y**, **1-Gd**), 2 (**2-Y**, **2-Gd**)). Chemical structure (left) of the binucleating ligand H_6BzN_6-Mes, which possesses a central benzene ring with trigonal symmetry and six aniline nitrogen atoms arranged with three nitrogen donors above the plane of the central ring and three below it. Crystal structure (right) of the $[Gd_2(BzN_6\text{-Mes})]^{2-}$ anion in **2-Gd**. Blue, grey and orange spheres represent N, C and Gd atoms, respectively; mesityl methyl groups, *tert*-butyl groups and H atoms are omitted for clarity.

bulk of the ligand and favourable electrostatic interactions between the benzene dianion and the metal cations.

The UV-vis spectra of **1-Y** and **1-Gd** are nearly identical from 400 to 800 nm, as are the spectra of **2-Y** and **2-Gd** (Extended Data Figs. 1 and 2). These results support ligand-based reduction, as UV-vis spectra for isostructural Y^{2+} or Gd^{2+} complexes typically feature large differences in the positions of their absorption maxima[28]. Structures of **1-Gd**, **2-Y** and **2-Gd** determined by single-crystal X-ray diffraction provide further evidence of ligand-based reduction (Fig. 1 and Supplementary Figs. 32–35; data for **1-Y** were consistently of low resolution, precluding meaningful analysis). The average M–N distances for **2-Y** and **2-Gd** are 2.281(2) and 2.309(2) Å, respectively, within the range typically observed for Y^{3+} and Gd^{3+} ions[29]. In **2-Y** and **2-Gd**, the average C–C distance of the central benzene ring is 1.442(6) and 1.442(5) Å, respectively, longer than the corresponding distance of 1.423(11) Å in **1-Gd** and the average of 1.40 Å in neutral benzene. This central ring is also planar in **1** and **2**, as evidenced by small C_4–C_5–C_1–C_2 torsion angles of $|\theta| \leq 1.4°$ (Supplementary Table 2). Comparing the structure of the BzN_6-Mes ligand in **1-Gd** and **2-Gd**, the only bond distance changes occur in the central benzene ring, suggesting that spin density is localized there. This result was confirmed by a density functional theory (DFT) analysis of **2-Y** (Extended Data Fig. 3).

EPR spectroscopy. High-frequency EPR spectra were collected at 371 GHz from 5 to 200 K on a polycrystalline sample of **2-Y**. The spectra display a nearly isotropic *g*-tensor centred at 2.00. However, a half-field transition—characteristic of an $S = 1$ state—was not observed (Extended Data Fig. 4). To confirm that the EPR signal in **2-Y** results from an $S = 1$ state, we carried out electron-spin nutation experiments on frozen solutions of **1-Y** and **2-Y** at D-band frequencies (Fig. 2a). The nutation frequency in this experiment is determined by the spin-transition matrix element and thus the difference in oscillation period for two molecules can be used to determine their relative spin quantum numbers[30]. The oscillation periods for **1-Y** and **2-Y** differ by a factor of $\sqrt{2}$, as expected for total spins of $S = 1/2$ and $S = 1$, respectively.

A modified Bleaney–Bowers equation (see equation (S1) in the Supplementary Information) was used to fit the temperature dependence of the EPR signal intensity (Fig. 2b and Extended Data Figs. 5 and 6)[31]. The analysis revealed a singlet ground state with a singlet–triplet gap of $\Delta E_{ST} = 0.025(4)$ kcal mol^{-1} (8.7(1.4) cm^{-1}) for **2-Y**, which is corroborated by DFT calculations (Supplementary Table 6). This value is substantially smaller than that typically observed for annulenes with $4n$ π electrons and can be attributed to the trigonal symmetry and rigidity of **2-Y**, which energetically disfavours quinoidal distortion. The powerful impact of these effects is apparent from comparisons with ΔE_{ST} values reported for other benzene dianions: D_{2h}-symmetric 1,2,4,5-$C_6H_2(SiMe_3)_4^{2-}$ shows a strong quinoidal distortion and a singlet–triplet gap that is too large to measure, while trigonal $C_6(SiMe_2CH_2SiMe_2)_3^{2-}$ shows a less severe distortion and a ΔE_{ST} of 1.0 kcal mol^{-1} (refs. [32,33]).

Magnetism and electronic structure analysis. We hypothesized that the triplet state could be further stabilized through magnetic exchange with Gd^{3+}, given that coupling with spin-bearing metal ions is significantly stronger for open-shell triplets than closed-shell singlets[34]. Significantly, d.c. magnetic susceptibility data for **2-Gd** between 2 and 300 K are indicative of an $S = 6$ ground state, arising from antiferromagnetic coupling between the $S = 1$ bridging benzene dianion and two $S = 7/2$ Gd^{3+} ions (Fig. 3a and Extended Data Figs. 7 and 8). The susceptibility data were fitted with a spin-only Hamiltonian, which yielded an average exchange coupling constant of $J_{Gd\text{–}rad} = -43$ cm^{-1}, representing the strongest coupling observed to date for any Ln^{3+}–ligand interaction[34]. We note that it is important to differentiate **2-Gd** from transition metal or actinide annulene complexes, in which the ligand π electrons form strong covalent bonds with the metal ion(s) and oxidation state is often ambiguous[35,36]. By contrast, the valence electrons in **2-Gd** are well-isolated due to the contracted nature of the 4*f* orbitals and do not engage in covalent bonding, instead favouring metal–ligand magnetic coupling and preservation of the dianion π system[34]. Thus, lanthanide ions are particularly well-suited to stabilize the triplet benzene dianion via exchange coupling, without perturbing its aromaticity.

The relative energy of the benzene dianion singlet and triplet states in **2-Gd** can be estimated using the ΔE_{ST} value established for **2-Y**, while the interactions of the dianion with the Gd^{3+} ions can be evaluated from the magnetic data for **2-Gd** (Fig. 3; see also 'Electronic Structure Analysis for **2-Gd**' in the Supplementary Information). This analysis revealed that the $S = 6$ ground state of

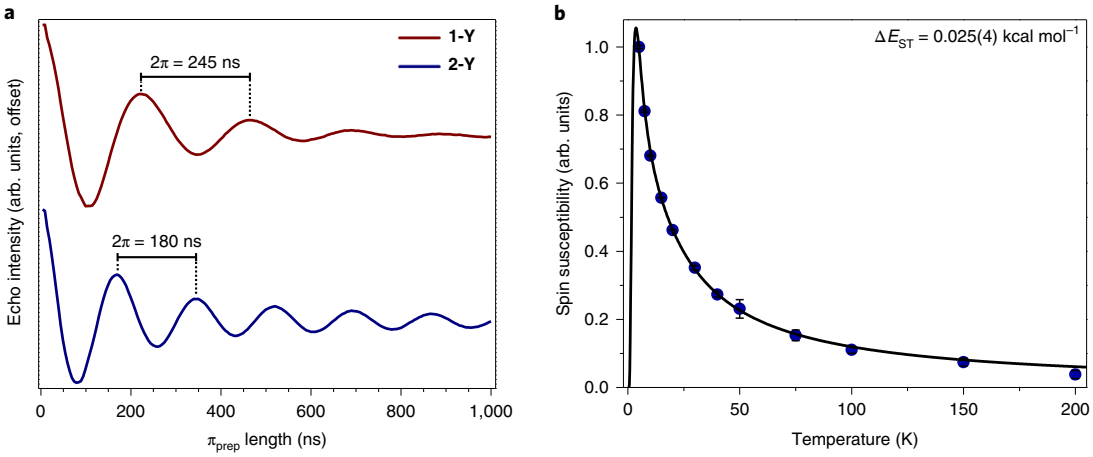

Fig. 2 | Electron paramagnetic resonance spectroscopy data. a, Electron-spin nutation data for frozen solutions of **1-Y** and **2-Y**. The difference in oscillation period is consistent with an $S = 1$ state in **2-Y**. **b**, Temperature dependence of the EPR spin susceptibility for a polycrystalline sample of **2-Y** (blue circles) fitted to a modified Bleaney–Bowers equation (black line). Error bars represent the deviation away from zero of the double integrated area intensity in the field region where no EPR signal is observed.

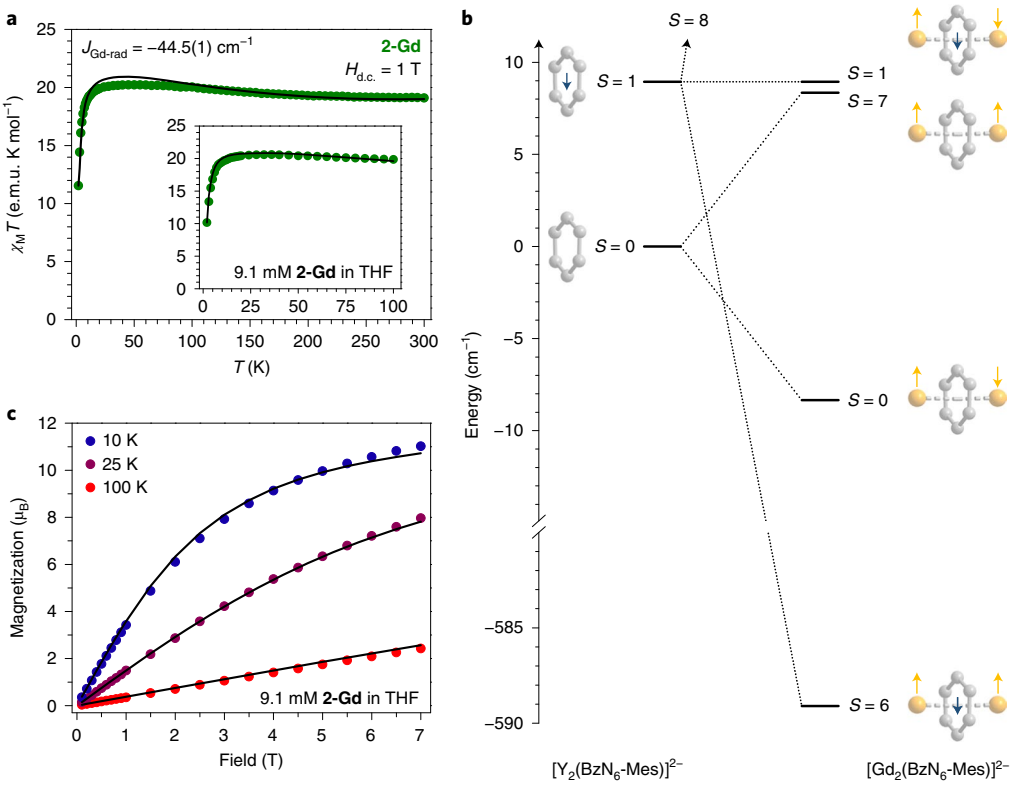

Fig. 3 | Electronic structure analysis. a, Fit of the d.c. magnetic susceptibility data for **2-Gd** (green circles) to a spin-only Hamiltonian (black line). Fits to data collected under an applied magnetic field ($H_{d.c.}$) of 0.1, 0.5 and 1 T for a polycrystalline sample of **2-Gd** gave an average exchange coupling constant of $J_{Gd\text{-}rad} = -43\,cm^{-1}$, while a fit to data collected for a frozen solution (inset), wherein intermolecular interactions are negligible, gave $J_{Gd\text{-}rad} = -50(4)\,cm^{-1}$. **b**, Electronic states of $[Y_2(BzN_6\text{-}Mes)]^{2-}$ in **2-Y** (left), with ΔE_{ST} determined by EPR spectroscopy and of $[Gd_2(BzN_6\text{-}Mes)]^{2-}$ in **2-Gd** (right), determined from experimental magnetic susceptibility data. Arrows represent the spins of the Gd^{3+} ions (orange) or the benzene ring (blue). The $S = 1$ state of the benzene dianion is preferentially stabilized relative to the $S = 0$ state through antiferromagnetic coupling to the $S = 7/2$ Gd^{3+} ions, resulting in an overall $S = 6$ ground state. **c**, Fit of magnetization data for **2-Gd** (coloured circles) to an $S = 6$ Brillouin function (black line). The $S = 6$ ground state is populated up to at least 100 K, consistent with the electronic structure diagram.

2-Gd is stabilized by as much as −1.7 kcal mol^{-1} (−580 cm^{-1}) relative to the first excited state (Fig. 3b). Significantly, this stabilization is much larger than that observed for other $4n$ π-electron annulenes with a triplet ground state ($|\Delta E_{ST}| \leq 0.008$ kcal mol^{-1}) and enables direct observation and characterization of elusive ground-state Baird aromaticity[26,27].

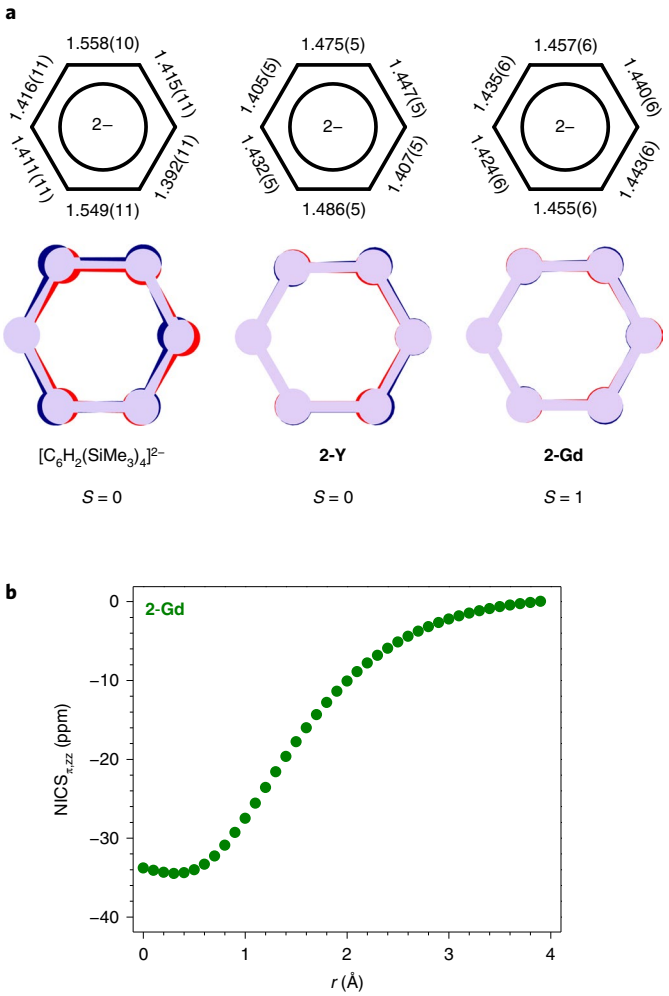

Fig. 4 | Baird aromaticity in $[Gd_2(BzN_6\text{-Mes})]^{2-}$. a, Bond distances (Å) in the dianionic benzene ring from the crystal structures of [Li(dimethoxyethane)]$_2$[$C_6H_2(SiMe_3)_4$], **2-Y** and **2-Gd** (top) and comparison of these crystal structures (blue) and an idealized D_{6h}-symmetric benzene ring (red) highlighting overlap (purple) (bottom)[33]. For **2-Gd** the bond length equalizations are characteristic of an aromatic ring. **b**, Calculated out-of-plane component of the chemical shift arising from only the π molecular orbitals ($NICS_{\pi,zz}$) along the z axis for the experimentally determined structure of the central benzene dianion in **2-Gd**. The negative values obtained for **2-Gd** are indicative of aromaticity[38–40].

Analysis of aromaticity. Aromaticity in the singlet and triplet states of the benzene dianion can be analysed by comparing the crystal structures of **2-Y** and **2-Gd**. The benzene dianion in **2-Y** ($S=0$) is distorted, with C–C distances ranging from 1.405(5) to 1.486(5) Å and a standard deviation of 0.031 Å, suggestive of a non-aromatic state. By contrast, the C–C bond distances of the benzene dianion in **2-Gd** ($S=1$) exhibit a much smaller standard deviation of only 0.011 Å, revealing bond length equalization characteristic of an aromatic ring (Fig. 4a and Supplementary Fig. 36). The standard deviation in **2-Gd** is also significantly smaller than that observed for singlet benzene dianions reported in the literature[32,33]. The average C–C bond distance in **2-Gd**, 1.442(6) Å, is consistent with the value determined for **2-Y**, 1.442(5) Å, and longer than the value predicted for a free triplet benzene dianion by DFT calculations, 1.391 Å (see Supplementary Tables 2 and 7 for additional structural comparisons).

NMR spectroscopy can also be used as an experimental probe of aromaticity, but it was not possible to identify resonances associated with the hydrogen atoms of the benzene dianion in **2-Y** and **2-Gd** due to the paramagnetism of the triplet state. Instead, nucleus-independent chemical shift (NICS) calculations were carried out to probe the aromaticity in **2-Gd** and **2-Y**, using the experimentally determined structure of the central benzene dianion in each complex[37]. In this technique, the magnetic shielding is calculated for a virtual nucleus located at position x relative to a ring (for example, in the centre or directly above) and the magnitude and sign of this value is used to determine aromaticity. Positive and negative chemical shift values indicate antiaromaticity and aromaticity, respectively, while values close to zero are indicative of non-aromatic character. Isotropic NICS(0) values of 0.5 and −9.1 ppm obtained for **2-Y** and **2-Gd**, respectively, are consistent with our analysis of the structural data. Isotropic NICS calculations carried out on the entire $[Gd_2(BzN_6\text{-Mes})]^{2-}$ complex in **2-Gd** corroborate these results (Supplementary Table 8). The out-of-plane component of the NMR tensor arising from only the π molecular orbitals, $NICS_{\pi,zz}$, was also calculated at distances along the z axis from 0 to 3.9 Å for **2-Gd** using the experimentally determined structure of the central benzene dianion (Fig. 4b and Supplementary Fig. 42), yielding a $NICS(1)_{\pi,zz}$ value of −29.8(1.9) ppm and a $\int NICS_{\pi,zz}$ value of −138.0(16.9) ppm (Supplementary Fig. 44)[38–41]. According to this analysis, **2-Gd** possesses a diatropic ring current that is ~30% larger than the ring current in benzene[41]. Calculations performed on a free triplet benzene dianion with an optimized geometry yield values similar to those determined for **2-Gd** (Supplementary Figs. 43 and 45 and Supplementary Tables 9 and 10).

Calculations employing a harmonic oscillator model of aromaticity were also performed with the experimentally determined structures of **2-Y** and **2-Gd** (ref. [42]). This method compares the normalized sum of squared deviations of bond lengths in an annulene to a calculated optimal value, with a value of 1 indicating aromaticity and a value of 0 indicating non-aromatic character. Values of −0.07 and 0.46 were obtained for **2-Y** and **2-Gd**, respectively, further supporting our assignment of the singlet state as non-aromatic and the triplet state as aromatic.

Conclusions

The foregoing analysis demonstrates how molecular symmetry, rigidity and even magnetic exchange coupling can be leveraged to preferentially stabilize and study a desired electronic state in an organic molecule. Significantly, this approach enables the isolation of a benzene dianion in which the triplet state—typically a high-energy excited state in monocyclic π systems—instead exists as the well-isolated molecular ground state, enabling direct observation of its aromaticity.

Online content

Any methods, additional references, Nature Research reporting summaries, source data, extended data, supplementary information, acknowledgements, peer review information; details of author contributions and competing interests; and statements of data and code availability are available at https://doi.org/10.1038/s41557-021-00737-8.

Received: 16 June 2020; Accepted: 20 May 2021;
Published online: 19 July 2021

References

1. Anslyn, E. V. & Dougherty, D. A. *Modern Physical Organic Chemistry* (University Science Books, 2006).
2. Gleiter, R. *Aromaticity and Other Conjugation Effects* (Wiley-VCH, 2012).
3. Dewar, M. J. S. Aromaticity and pericyclic reactions. *Angew. Chem. Int. Ed.* **10**, 761–776 (1971).
4. Fallon, K. J. et al. Exploiting excited-state aromaticity to design highly stable singlet fission materials. *J. Am. Chem. Soc.* **141**, 13867–13876 (2019).
5. Randić, M. Aromaticity of polycyclic conjugated hydrocarbons. *Chem. Rev.* **2003**, 3449–3605 (2003).

6. Hückel, E. Quantentheoretische Beiträge zum Benzolproblem. I. Die Elektronenkonfiguration des Benzols und verwandter Verbindungen. *Z. Phys.* **70**, 204–286 (1931).
7. Breslow, R., Brown, J. & Gajewski, J. J. Antiaromaticity of cyclopropenyl anions. *J. Am. Chem. Soc.* **89**, 4383–4390 (1967).
8. Heilbronner, E. Hückel molecular orbitals of Möbius-type conformations of annulenes. *Tetrahedron* **5**, 1923–1928 (1964).
9. Herges, R. Topology in chemistry: designing Möbius molecules. *Chem. Rev.* **106**, 4820–4842 (2006).
10. Rappaport, S. M. & Rzepa, H. S. Intrinsically chiral aromaticity. Rules incorporating linking number, twist, and writhe for higher-twist Möbius annulenes. *J. Am. Chem. Soc.* **130**, 7613–7619 (2008).
11. Baird, N. C. Quantum organic photochemistry. II. Resonance and aromaticity in the lowest $^3\pi\pi^*$ state of cyclic hydrocarbons. *J. Am. Chem. Soc.* **94**, 4941–4948 (1972).
12. Ottosson, H. Exciting excited-state aromaticity. *Nat. Chem.* **4**, 969–971 (2012).
13. Rosenberg, M., Dahlstrand, C., Kilså, K. & Ottosson, H. Excited state aromaticity and antiaromaticity: opportunities for photophysical and photochemical rationalizations. *Chem. Rev.* **114**, 5379–5425 (2014).
14. Wan, P. & Krogh, E. Evidence for the generation of aromatic cationic systems in the excited state. Photochemical solvolysis of fluoren-9-ol. *J. Chem. Soc. Chem. Commun.* 1207–1208 (1985).
15. Ueda, M. et al. Energetics of Baird aromaticity supported by inversion of photoexcited chiral [4*n*]annulene derivatives. *Nat. Commun.* **8**, 346 (2017).
16. Kim, J. et al. Two-electron transfer stabilized by excited-state aromatization. *Nat. Commun.* **10**, 4983 (2019).
17. Kostenko, A. et al. Spectroscopic observation of the triplet diradical state of cyclobutadiene. *Angew. Chem. Int. Ed.* **56**, 10183–10187 (2017).
18. Oh, J., Sung, Y. M., Hong, Y. & Kim, D. Spectroscopic diagnosis of excited-state aromaticity: capturing electronic structure and conformations upon aromaticity reversal. *Acc. Chem. Res.* **51**, 1349–1358 (2018).
19. Hada, M. et al. Structural monitoring of the onset of excited-state aromaticity in a liquid crystal phase. *J. Am. Chem. Soc.* **139**, 15792–15800 (2017).
20. Sung, Y. M. et al. Reversal of Hückel anti(aromaticity) in the lowest triplet states of hexaphyrins and spectroscopic evidence for Baird's rule. *Nat. Chem.* **7**, 418–422 (2015).
21. Fratev, F., Monev, V. & Janoschek, R. *Ab initio* study of cyclobutadiene in excited states: optimized geometries, electronic transitions and aromaticities. *Tetrahedron* **38**, 2929–2932 (1982).
22. Ni, Y. et al. 3D global aromaticity in a fully conjugated diradicaloid cage at difference oxidation states. *Nat. Chem.* **12**, 242–248 (2020).
23. Cha, W.-Y. et al. Bicyclic Baird-type aromaticity. *Nat. Chem.* **9**, 1243–1248 (2017).
24. Valiev, R. R., Fliegl, H. & Sundholm, D. Bicycloaromaticity and Baird-type bicycloaromaticity of dithienothiophene-bridged [34]octaphyrins. *Phys. Chem. Chem. Phys.* **20**, 17705–17713 (2018).
25. Falceto, A., Casanova, D., Alemany, P. & Alvarez, S. Distortions of π-coordinated arenes with anionic character. *Chem. Eur. J.* **20**, 14674–14689 (2014).
26. Breslow, R., Hill, R. & Wasserman, E. Pentachlorocyclopentadienyl cation, a ground-state triplet. *J. Am. Chem. Soc.* **86**, 5349–5350 (1964).
27. Wasserman, E., Hutton, R. S., Kuck, V. J. & Chandross, E. A. Dipositive ion of hexachlorobenzene, a ground-state triplet. *J. Am. Chem. Soc.* **96**, 1965–1966 (1974).
28. MacDonald, M. R., Bates, J. E., Ziller, J. W., Furche, F. & Evans, W. J. Completing the series of +2 ions for the lanthanide elements: synthesis of molecular complexes of Pr^{2+}, Gd^{2+}, Tb^{2+}, and Lu^{2+}. *J. Am. Chem. Soc.* **135**, 9857–9868 (2013).
29. Groom, C. R., Bruno, I. J., Lightfoot, M. P. & Ward, S. C. The Cambridge Structural Database. *Acta. Cryst.* **72**, 171–179 (2016).
30. Astashkin, A. V. & Schweiger, A. Electron-spin transient nutation: a new approach to simplify the interpretation of ESR spectra. *Chem. Phys. Lett.* **174**, 595–602 (1990).
31. Bleaney, B. & Bowers, K. D. Anomalous paramagnetism of copper acetate. *Proc. Roy. Soc. A.* **214**, 451–465 (1952).
32. Ebata, K. et al. Planar hexasilylbenzene dianion with thermally accessible triplet state. *J. Am. Chem. Soc.* **120**, 1335–1336 (1998).
33. Sekiguchi, A., Ebata, K., Kabuto, C. & Sakurai, H. Bis[(dimethoxyethane) lithium(I)] 1,2,4,5-tetrakis(trimethylsilyl)benzenide. The first 6C-8π antiaromatic benzene dianion. *J. Am. Chem. Soc.* **113**, 7081–7082 (1991).
34. Demir, S., Jeon, I.-R., Long, J. R. & Harris, T. D. Radical-ligand containing single-molecule magnets. *Coord. Chem. Rev.* **289–290**, 149–176 (2015).
35. Diaconescu, P. L., Arnold, P. L., Baker, T. A., Mindiola, D. J. & Cummins, C. C. Arene-bridged diuranium complexes: inverted sandwiches supported by δ backbonding. *J. Am. Chem. Soc.* **122**, 6108–6109 (2000).
36. Pampaloni, G. Aromatic hydrocarbons as ligands. Recent advances in the synthesis, reactivity and the applications of bis(η^6-arene) complexes. *Coord. Chem. Rev.* **254**, 402–419 (2010).
37. von Ragué Schleyer, P., Maerker, C., Dransfeld, A., Jiao, H. & van Eikema Hommes, N. J. R. Nucleus-independent chemical shifts: a simple and efficient aromaticity probe. *J. Am. Chem. Soc.* **118**, 6317–6318 (1996).
38. Stanger, A. Nucleus-independent chemical shifts (NICS): distance dependence and revised criteria for aromaticity and antiaromaticity. *J. Org. Chem.* **71**, 883–893 (2006).
39. Stanger, A. Obtaining relative induced ring currents quantitatively from NICS. *J. Org. Chem.* **75**, 2281–2288 (2010).
40. Gershoni-Poranne, R. & Stanger, A. The NICS-*XY*-scan: identification of local and global ring currents in multi-ring systems. *Chem. Eur. J.* **20**, 5673–5688 (2014).
41. Stanger, A. Reexamination of $NICS_{zzz}$: height dependence, off-center values, and integration. *J. Phys. Chem. A* **123**, 3922–3927 (2019).
42. Kruszewski, J. & Krygowski, T. M. Definition of aromaticity basing on the harmonic oscillator model. *Tetrahedron Lett.* **13**, 3839–3842 (1972).

Methods

General methods and materials. Unless otherwise specified, all reactions were carried out in flame-dried glassware under an argon atmosphere using standard Schlenk techniques or in an argon- or nitrogen-atmosphere glovebox. Commercial reagents were purchased from Sigma Aldrich, Fischer, Acros, Oakwood, Strem or Alfa Aesar and were used without further purification. *N*,*N*-dimethylformamide (DMF), THF, toluene and hexanes were sparged with argon and then dried by passing them through alumina columns in a Glass Contour solvent purification system from JC Meyer. 2-Bromo-5-*tert*-butylbenzene-1,3-dicarbaldehyde and $Y(CH_2SiMe_3)_3(THF)_2$ were prepared according to literature reports[43,44]. Elemental analyses (C, H, N) were performed by the Microanalytical Facility at the University of California, Berkeley using a Perkin Elmer 2400 Series II combustion analyser. Fourier transform infrared (FTIR) spectra were recorded on a Perkin Elmer Avatar Spectrum 400 FTIR Spectrometer equipped with an attenuated total reflectance (ATR) attachment. Matrix assisted laser desorption ionization time of tlight (MALDI-TOF) mass spectra were recorded on an Applied Biosystems Voyager-DE PRO Workstation in positive ion mode. Samples were co-crystallized in an anthracene matrix on an AB SCIEX MALDI-TOF stainless steel sample plate. Spectra were averaged over 200 laser pulses with a low-mass gate of 300 Da and a high-mass gate of 2,000 Da.

NMR spectroscopy. NMR spectroscopy data were obtained on solutions in deuterated solvents ($CDCl_3$, C_6D_6, or C_4D_8O) obtained from Cambridge Isotope Laboratories. ^{1}H NMR and ^{13}C NMR data were recorded on Bruker DRX-500 and AV-500 spectrometers. Chemical shifts (δ) are reported in ppm relative to the residual solvent peak (δ 7.26 for $CDCl_3$ and δ 7.16 for C_6D_6 for ^{1}H NMR; δ 77.16 for $CDCl_3$ and δ 128.06 for C_6D_6 for ^{13}C NMR). Data for ^{1}H NMR are reported in the following format: chemical shift (ppm) (multiplicity (s = singlet, d = doublet, m = multiplet), coupling constant (Hz), integration). Data for ^{13}C NMR are reported in terms of chemical shift (ppm).

Synthesis of 1,3,5-tris(4,4,5,5-tetramethyl-1,3,2-dioxaborolan-2-yl)benzene. This compound was prepared according to a modified literature procedure[45]. 1,3,5-Tribromobenzene (10.0 g, 31.8 mmol), bis(pinacolato)diboron (25.4 g, 100 mmol, 3.1 equiv.), potassium acetate (18.7 g, 190 mmol, 6 equiv.) and Pd(dppf)Cl_2 (870 mg, 1.19 mmol, 4 mol%) (dppf = 1,1′-ferrocenediyl-bis(diphenylphos phine)) were dissolved in 100 ml dry DMF in a Schlenk flask under argon. The resulting solution was heated to 90 °C for 24 h during which time it became black in colour. The solution was then cooled to room temperature and added to 1,200 ml H_2O in air. A greyish-black precipitate was collected by vacuum filtration, dissolved in ethyl acetate (EtOAc) and passed over a silica gel plug to yield a brown solution. The silica gel was then washed with additional EtOAc (~1,000 ml) and the combined filtrates were concentrated to yield a light brown powder. This solid was triturated in MeOH (200 ml), filtered off and washed with additional MeOH (3 × 50 ml) to yield the product as a colourless solid in 75% yield (10.8 g, 23.8 mmol).

Synthesis of 1,3,5-tris(2′,6′-dicarbaldehyde-4′-*tert*-butylphenyl)benzene. A 200 ml Schlenk flask was charged with a 1:1 dioxane/H_2O solution (150 ml) and the solvent was sparged for 15 min with argon. To this solution was added 1,3,5-tris(4,4,5,5-tetramethyl-1,3,2-dioxaborolan-2-yl)benzene (2.50 g, 5.48 mmol), 2-bromo-5-*tert*-butylbenzene-1,3-dicarbaldehyde (5.08 g, 18.9 mmol, 3.4 equiv.), K_3PO_4 (10.7 g, 50.6 mmol, 9.2 equiv.) and Pd(dppf)Cl_2 (300 mg, 0.410 mmol, 7.5 mol%). The resulting red solution was heated to 90 °C with stirring for 5 h; an abrupt colour change to yellow was observed roughly 15 min after the start of the reaction, followed by a gradual colour change to brown. The reaction was then cooled to room temperature and quenched in air with a saturated aqueous solution of NH_4Cl (200 ml). The resulting solution was extracted with CH_2Cl_2 (3 × 75 ml) and the organic layers were combined and dried over Na_2SO_4. The combined organic layers were concentrated to yield a dark brown solid that was purified by column chromatography on silica (R_f = 0.21, 15% EtOAc in hexanes) to give the product as a colourless solid in 64% yield (2.25 g, 3.50 mmol).

^{1}H NMR (500 MHz, $CDCl_3$): δ = 10.05 (s, 6H), 8.26 (s, 6H), 7.44 (s, 3H), 1.42 (s, 27H) ppm. ^{13}C NMR (125 MHz, $CDCl_3$): δ = 190.8, 153.1, 142.3, 134.9, 134.6, 132.3, 131.4, 35.3, 31.2 ppm. IR (ATR, neat): ν 2,973, 2,871, 2,837, 2,754, 1,735, 1,687, 1,554, 1,461, 1,388, 1,364, 1,235, 1,210, 1,112, 1,044, 975, 955, 906, 870, 829, 805, 733, 702, 632, 528, 493, 473 cm^{-1}. MALDI ToF MS *m*/z: 642.3 [M] $^+$, 613.3 [M − HC = O]$^+$, 584.3 [M − 2 HC = O]$^+$, 555.3 [M − 3 HC = O]$^+$, 526.3 [M − 4 HC = O]$^+$, 497.3 [M − 5 HC = O]$^+$, 468.3 [M − 6 HC = O]$^+$.

Synthesis of 1,3,5-tris[2′,6′-(*N*-mesityl)diminyl-4′-*tert*-butylphenyl]benzene. A 100 ml Schlenk flask was charged with 4 Å molecular sieves (15 g) and heated to 165 °C for 1 h. The flask was then evacuated on a Schlenk line and gently heated with a Bunsen burner until a constant vacuum was achieved (100 mTorr). The flask was then back-filled with argon and charged with 1,3,5-tris(2′,6′-dicarbaldehyde-4′-*tert*-butylphenyl)benzene (450 mg, 0.70 mmol), 2,4,6-trimethylaniline (1.80 ml, 12.8 mmol, 18 equiv. = 3 equiv. per aldehyde), acetic acid (0.5 ml) and toluene (15 ml). The resulting yellow solution was heated to 100 °C for 12 h with stirring. The reaction was then cooled to room temperature, the mixture filtered over Celite in air and the filter pad washed with EtOAc (30 ml). The eluent was concentrated to give a yellow oil and addition of MeOH (10 ml) to this oil resulted in precipitation of the product as a yellow solid in 86% yield (802 mg, 0.596 mmol). The product was collected by filtration and washed with additional MeOH (10 ml) and dried.

^{1}H NMR (500 MHz, C_6D_6): δ = 8.90 (s, 6H), 8.24 (s, 6H), 7.49 (s, 3H), 6.64 (s, 12H), 2.10 (s, 18H), 1.87 (s, 36H), 1.38 (s, 27H) ppm. ^{13}C NMR (125 MHz, C_6D_6): δ = 160.0, 152.2, 148.6, 139.8, 136.4, 135.4, 134.0, 133.2, 129.3, 127.2, 127.1, 35.2, 31.2, 20.8, 18.3 ppm. IR (ATR, neat): ν 2,964, 2,912, 2,858, 2,729, 1,697, 1,624, 1,478, 1,458, 1,439, 1,397, 1,375, 1,363, 1,297, 1,251, 1,236, 1,203, 1,146, 1,033, 1,012, 991, 965, 933, 899, 855, 827, 773, 738, 666, 641, 631, 609, 600, 581, 550, 523, 507 cm^{-1}. MALDI ToF MS *m*/z: 1,344.9 [M]$^+$, 1,211.8 [M − NC_9H_{11}]$^+$.

Synthesis of 1,3,5-tris[2′,6′-(*N*-mesityl)dimethanamino-4′-*tert*-butylphenyl] benzene (H_6BzN_6-Mes). A 100 ml Schlenk flask was charged with 1,3,5-tris[2′,6′-(*N*-mesityl)diminyl-4′-*tert*-butylphenyl]benzene (800 mg, 0.594 mmol) and THF (40 ml). The resulting yellow solution was cooled to 0 °C with stirring and a solution of $LiAlH_4$ (1.0 M in THF, 7.1 ml, 7.1 mmol, 12 equiv. = 2 equiv. per imine) was added dropwise. The reaction was then stirred for 1 h at 0 °C and allowed to warm to 25 °C over 1 h during which time the solution became deep orange-red. The reaction was next heated to 50 °C for 12 h. The solution was then cooled to 0 °C and quenched by dropwise addition of MeOH (10 ml), filtered over Celite in air and the filter pad was then washed with EtOAc (30 ml). The combined organics were concentrated to give light yellow solids which were triturated in hexanes (10 ml). The mixture was filtered over Celite, the filter pad was washed with additional hexanes (10 ml) and the combined eluents were concentrated to give the crude product as a light yellow oil. This oil was purified by column chromatography on deactivated silica (the column was first washed with 4:1:95 Et_3N/EtOAc/hexanes, then the crude product was loaded and eluted in 5% EtOAc in hexanes; R_f = 0.25) to give the product as a colourless solid in 64% yield (513 mg, 0.378 mmol). The product is highly soluble in a range of solvents and solidifies as a foam; to obtain a free-flowing powder it is necessary to dry it using a high vacuum for 1–2 h, preferably after it has been dissolved in hexanes.

^{1}H NMR (500 MHz, C_6D_6) δ = 7.52 (s, 6H), 7.33 (s, 3H), 6.70 (s, 12H), 4.12 (s, 12H), 2.18 (s, 18H), 1.99 (s, 36H), 1.24 (s, 27H) ppm. ^{13}C NMR (125 MHz, C_6D_6): δ = 150.7, 144.0, 140.1, 139.2, 137.3, 131.1, 130.3, 130.1, 129.9, 124.9, 51.8, 34.7, 31.3, 20.9, 18.6 ppm. IR (ATR, neat): ν 3,363, 2,952, 2,912, 2,863, 2,725, 1,726, 1,604, 1,588, 1,482, 1,444, 1,407, 1,362, 1,344, 1,302, 1,228, 1,201, 1,154, 1,071, 1,028, 1,010, 929, 883, 851, 763, 733, 696, 653, 561, 500, 466 cm^{-1}. MALDI ToF MS *m*/z: 1,357.0 [M]$^+$, 1,221.9 [M − HNC_9H_{11}]$^+$, 1,096.8 [M − 2 HNC_9H_{11}]$^+$, 951.7 [M − 3 HNC_9H_{11}]$^+$, 816.6 [M − 4 HNC_9H_{11}]$^+$, 681.5 [M − 5 HNC_9H_{11}]$^+$, 546.4 [M − 6 HNC_9H_{11}]$^+$.

Synthesis of [Y_2(BzN_6-Mes)][K(18-crown-6)(THF)$_2$]$_2$ (2-Y). In an argon-atmosphere glovebox, ligand H_6BzN_6-Mes (100 mg, 0.0736 mmol) was placed in a 4 ml scintillation vial and dissolved in benzene (3 ml). The solution was added dropwise with stirring to a solution of $Y(CH_2SiMe_3)_3(THF)_2$ (72.9 mg, 0.147 mmol, 2.1 equiv.) in benzene (4 ml) in a 20 ml scintillation vial. The mixture turned yellow gradually over the course of ligand addition. The resulting solution was stirred for 3 h and then concentrated to yield yellow solids. At 25 °C, a solution of 18-crown-6 (38.1 mg, 0.144 mmol, 1 equiv.) in THF (4 ml) was added to these solids followed immediately by addition of KC_8 (19.5 mg, 0.144 mmol, 1 equiv.), which resulted in a solution colour change to deep blue-black. The resulting solution was stirred for 10 min. The reaction mixture was then filtered over Celite and concentrated to 1.5 ml, layered with hexanes (1.5 ml) and stored at room temperature (25 °C) for 3 h. The product precipitated as dark blue-black polycrystals (88.8 mg, 50% yield). This complex decomposes in solution at 25 °C, but is indefinitely stable when stored as a solid. It was stored as a solid under inert atmosphere at −30 °C. Block-shaped crystals suitable for X-ray diffraction were grown from a THF/hexane solution stored for 12 h at room temperature (25 °C).

IR (ATR, neat): ν 2,950, 2,903, 2,859, 1,604, 1,481, 1,394, 1,330, 1,298, 1,285, 1,246, 1,232, 1,198, 1,152, 1,105, 1,029, 1,009, 961, 883, 868, 851, 785, 734, 672, 582, 561, 530, 511, 502 cm^{-1}. MALDI ToF MS *m*/z: 1,528.7 [M]$^+$, 1,439.8 [M − Y]$^+$, 1,351.0 [M − 2 Y]$^+$. Analysis calculated for $C_{116}H_{154}KN_6O_8Y_2$: C, 67.36; H, 8.06; N, 3.47; found: C, 67.23; H, 8.10; N, 3.74.

Synthesis of [Gd_2(BzN_6-Mes)][K(18-crown-6)(THF)$_2$]$_2$ (2-Gd). In an argon-atmosphere glovebox, $GdCl_3$·2.5THF (54.9 mg, 0.124 mmol, 2 equiv.) and $Li(CH_2SiMe_3)$ (35.0 mg, 0.372 mmol, 6 equiv.) were placed in a 20 ml scintillation vial with a Teflon-coated stir bar and suspended in pre-cooled hexanes (6 ml, −30 °C). The vial was placed in a cold well (cooled with an ice/brine bath at approximately −20 °C) and the resulting slurry was stirred for 3 h, at which point a solution of H_6BzN_6-Mes (84.0 mg, 0.0619 mmol, 1 equiv.) in benzene (2 ml) was added dropwise. The slurry immediately became a bright yellow solution with colourless solids. After the addition was complete, the reaction mixture was stirred for 3 h at 25 °C. The solvent was then removed under reduced pressure and the resulting solids were extracted with hexanes (6 ml). The hexanes extract was filtered and concentrated to yield a yellow solid. The yellow solids were dissolved in THF (3 ml) in a 20 ml scintillation vial equipped with a Teflon-coated stir bar. A solution of 18-crown-6 (32.0 mg, 0.121 mmol, 2 equiv.) in THF (2 ml) was added to the resulting yellow solution. To this yellow solution was added KC_8 (16.4 mg,

0.121 mmol, 2 equiv.) and the resulting deep blue/black solution was stirred for 10 min. The reaction mixture was then filtered and concentrated to 1.5 ml, layered with hexanes (1.5 ml) and stored at 25 °C for 3 h. The product precipitated as dark blue-black polycrystals (67.2 mg, 42% yield). This complex decomposes in solution at 25 °C although it is indefinitely stable when stored as a solid. It was stored as a solid under inert atmosphere at −30 °C. Block-shaped crystals suitable for X-ray diffraction were grown from a THF/hexane solution stored for 12 h at room temperature (25 °C).

IR (ATR, neat): ν 2,951, 2,902, 2,860, 1,602, 1,480, 1,469, 1,394, 1,360, 1,352, 1,297, 1,231, 1,200, 1,152, 1,104, 1,018, 961, 883, 867, 852, 786, 734, 671, 589, 587, 560, 529, 503, 493 cm^{-1}. MS *m*/z: 1,666.8 $[M]^+$, 1,508.8 $[M - Gd]^+$, 1,350.9 $[M - 2 Gd]^+$. Analysis calculated for $C_{136}H_{194}K_2N_6O_{16}Gd_2$: C, 63.76; H, 7.63; N, 3.28; found: C, 63.56; H, 7.57; N, 3.64.

UV-vis-near infrared spectroscopy. UV-vis-near infrared (NIR) absorption spectra were collected with a CARY 5000 spectrophotometer interfaced with Varian WinUV software. Extinction coefficients for each feature in the spectra for **1** and **2** were extracted from plots of absorbance versus concentration. UV-vis spectra were also collected at 30 min intervals for THF solutions of **2-Y** and **2-Gd** at 25 °C for a period of 720 min to monitor decomposition rates for these compounds. Plots of ln[concentration] versus time for **2-Y** and **2-Gd** were linear and thus the data were fitted to a first-order rate law to extract half-life values.

Crystallography. Single crystals of **1** and **2** were coated in Paratone-N oil in an argon-atmosphere glovebox and mounted on Kaptan loops. X-ray diffraction data were collected at UC Berkeley using a Rigaku XtaLAB p200 equipped with a MicroMax-007 HF microfocus rotating anode and a Pilatus 200 K hybrid pixel array detector for **1-Y**, **2-Gd** and **2-Y** and a Bruker QUAZAR diffractometer equipped with a Bruker AXS Apex II detector for **1-Gd**. Data were collected at 100 K under a N_2 stream from an Oxford Cryosystems Cryostream with Mo Kα radiation (graphite monochromator). The frames were integrated with CrysAlis^{Pro} software, including a multi-scan absorption correction that was applied using the SCALE3 ABSPACK scaling algorithm within CrysAlis^{Pro} for **1-Y**, **2-Gd** and **2-Y** (ref. [46]). For **1-Gd**, raw data were integrated and Lorentz and polarization corrections were calculated and applied using Bruker AXS SAINT software[47]. The absorption correction was calculated and applied using SADABS (ref. [48]). Initial structure solutions for **1** and **2** were determined using direct methods (SHELXT) and refinements were carried out using SHELXL-2014 (ref. [49]).

EPR spectroscopy measurements. Continuous-wave high-field/frequency EPR (CW-EPR) data were collected on a home-built homodyne spectrometer outfitted with a 15/17 T Oxford magnet. Measurements were carried out in the frequency range from 28 to 370 GHz; microwaves were generated by harmonic multiplication using a Virginia Diodes Inc. multiplier chain, then propagated to and from the sample by oversized cylindrical light pipes. The field-modulated transmission signal was detected using a wide-band InSb bolometer[50]. D-band (130 GHz) EPR experiments were performed at the CalEPR facility in the Britt lab at the University of California, Davis on a home-built 130 GHz EPR spectrometer equipped with an 8 T cryogen-free magnet (Cryogenic Limited)[51]. A single phase-locked dielectric resonator oscillator at 7.647 GHz serves as the base frequency and it is mixed and multiplied up to 32.5 GHz and provides 0 dBm (1 mW) input power to the high-power side of the transmitter arm. Microwaves are generated at 130 GHz by amplification and multiplication of the 32.5 GHz microwaves using an amplifier–multiplier chain fabricated by Virginia Diodes Inc. The amplifier–multiplier chain pulse output power at 130 GHz is 23.2 dBm (210 mW), as measured by Virginia Diodes Inc. The sample probe is equipped with a TE_{011} mode cylindrical resonant cavity, designed and manufactured by HF EPR Instruments, Inc. (V. Krymov). The system is equipped with an Oxford-CF935 liquid helium cryostat and an ITC-503 temperature controller.

Magnetic measurements. Samples were prepared in an argon-atmosphere glovebox by first adding crystalline powder (11.2 mg of **1-Gd** or 20.4 mg of **2-Gd**) to a 5 mm inner diameter/7 mm outer diameter quartz tube with a raised quartz platform. A layer of eicosane was then added to the samples (18.1 mg for **1-Gd** and 21.4 mg for **2-Gd**) to provide good thermal contact between the sample and the bath and to prevent crystallite torqueing. The tubes were fitted with Teflon sealable adapters, evacuated using a glovebox vacuum pump and then flame-sealed with an O_2/H_2 flame under reduced pressure. After flame-sealing, the eicosane was melted in a 40 °C water bath. Magnetic measurements were also conducted on a 9.1 mM frozen solution of **2-Gd** in 1:1 THF/2MeTHF to ensure that the observed magnetic properties were molecular in origin and not due to long-range interactions in the solid state. Magnetic susceptibility measurements were collected using a Quantum Design MPMS2 SQUID magnetometer. The values reported for d.c. magnetic susceptibility and magnetization data are the mean of three measurements and the standard deviation for these data is quite small. As a result, error bars are smaller than the size of the data points in the magnetism plots in this manuscript and were thus omitted. All data were corrected for diamagnetic contributions from the core diamagnetism and for the diamagnetism of the eicosane used to suspend the sample, estimated using Pascal's constants to give corrections of $\chi_{dia} = -0.00124$ e.m.u. mol^{-1} and -0.00152 e.m.u. mol^{-1} for **1-Gd** and **2-Gd**, respectively. Fits to the d.c. susceptibility data were performed using PHI (ref. [52]), using the spin-only Hamiltonian $\hat{H} = -2J_{Gd-rad}\hat{S}_{rad}(\hat{S}_{Gd(1)} + \hat{S}_{Gd(2)})$, where J_{Gd-rad} represents the magnetic exchange coupling between each Gd^{3+} ion and the organic radical spin. $\hat{S}_{rad}$ values of ½ and 1 were used for fits to **1-Gd** and **2-Gd**, respectively. Contributions for temperature-independent paramagnetism and intermolecular coupling were included when fitting susceptibility measurements for solid samples.

DFT calculations. All DFT calculations were carried out with the ORCA 4.2.1 program[53]. Isotropic NICS calculations were performed using a PBE0 or B3LYP functional with the def2-SVP basis set within the ORCA program[37]. A dummy atom was employed in the centre of the central benzene ring and two more positions perpendicular to the ring, 0.5 and 1.0 Å, were also calculated. The X-ray-determined structure was used in the calculation without optimization. Calculations were performed on only the six atoms of the central benzene ring in **2-Y** and **2-Gd** using the B3LYP functional, as the $[M_2(BzN_6\text{-Mes})]^{2-}$ complex contains 104 non-hydrogen atoms and is therefore quite time-intensive and challenging to investigate. NICS calculations were also performed on the entire $[Gd_2(BzN_6\text{-Mes})]^{2-}$ complex in the structure of **2-Gd** to corroborate these results. The PBE0 functional was used for this calculation. $NICS_{\pi,zz}$ calculations were performed with the Guassian 09 program using the Aroma plugin package with the B3LYP functional and the AUG-CC-PVTZ basis set[54,55]. Calculations were performed on only the six atoms of the central benzene ring in **2-Gd** with positions determined by the X-ray structure and a free triplet benzene dianion with an optimized geometry. Values of $NICS_{\pi,zz}$ and 3Δiso were calculated at distances along the *z* axis ranging from 0 to 3.9 Å. The $NICS_{\pi,zz}$ and 3Δiso data from 1.0 to 3.9 Å were fitted to a third degree polynomial function, which was used to determine the value of NICS(1)$_{\pi,zz}$ (ref. [41]). The $NICS_{\pi,zz}$ and 3Δiso data from 2.0 to 3.9 Å were also fitted to the equation $NICS_{\pi,zz}(r) = BC^r$, where *r* is the distance from the centre of the ring along the *z* axis and *B* and *C* are free variables. Integration of this equation from 0 to 100 Å yielded the value of $\int NICS_{\pi,zz}$ (ref. [41]). The harmonic oscillator model of aromaticity (HOMA) index was calculated for **2-Y** and **2-Gd** by using the following formula[42]:

$$\mathrm{HOMA} = 1 - \frac{\alpha}{n}\sum_{i=1}^{n}\left(R_i - R_{\mathrm{opt}}\right)^2$$

where *n* is the number of C–C bonds in the benzene ring, R_i and R_{opt} correspond to the *i*th bond length in the analysed ring and the reference optimized benzene ring and $\alpha = 257.7$ Å^{-2} is a normalization factor. The DFT-optimized structures for **2-Y** and **2-Gd** at the BP-RI/def2-SVP level of theory were used for the calculations of HOMA indexes, as were the experimentally determined crystal structures.

Data availability

Crystallographic data for the structures in this Article have been deposited at the Cambridge Crystallographic Data Centre under deposition numbers CCDC 2012304 (**1-Y**), 2012306 (**2-Y**), 2012305 (**1-Gd**) and 2012307 (**2-Gd**). Copies of data can be obtained free of charge from www.ccdc.cam.ac.uk/structures. Additional synthetic methods, nuclear magnetic resonance spectra, UV-vis-NIR spectra, single crystal X-ray diffraction data, EPR spectra, magnetism data and computational details are available in the Supplementary Information and Extended Data. Source data for Supplementary Figs. 20 and 22–31 and input files for computations are also provided as Supplementary Data 5 and 6. Source data are provided with this paper.

References

43. Klingele, M. H. & Kersting, B. Z. Efficient medium-scale synthesis of 2-bromo-5-*tert*-butylbenzene-1,3-dicarbaldehyde. *Z. Naturforsch.* **56b**, 437–439 (2001).
44. Lappert, M. F. & Pearce, R. Stable silylmethyl and neopentyl complexes of scandium(III) and yttrium(III). *J. Chem. Soc. Chem. Commun.* 126 (1973).
45. Liu, Y., Niu, F., Lian, J., Zeng, P. & Niu, H. Synthesis and properties of starburst amorphous molecules: 1,3,5-tris(1,8-naphthalimide-4-yl)benzenes. *Synth. Met.* **160**, 2055–2060 (2010).
46. CrysAlisPro Software System v.1.171.39.7a (Rigaku Corporation, 2015).
47. SAINT and APEX 2 Software for CCD Diffractometers (Bruker Analytical X-ray Systems Inc., 2014).
48. Sheldrick, G. M. SADABS v.2.03 (Bruker Analytical X-ray Systems Inc., 2000).
49. Sheldrick, G. M. SHELXT and SHELXL (University of Göttingen, 2015).
50. Hassan, A. K. et al. Ultrawide band multifrequency high-field EMR technique: a methodology for increasing spectroscopic information. *J. Magn. Reson.* **142**, 300–312 (2000).
51. Oyala, P. H. et al. Biophysical characterization of fluorotyrosine probes site-specifically incorporated into enzymes: *E. coli* ribonucleotide reductase as an example. *J. Am. Chem. Soc.* **138**, 7951–7964 (2016).

52. Chilton, N. F., Anderson, R. P., Turner, L. D., Soncini, A. & Murray, K. S. PHI: a powerful new program for the analysis of anisotropic monomeric and exchange-coupled polynuclear *d*- and *f*-block complexes. *J. Comput. Chem.* **34**, 1164–1175 (2013).
53. Neese, F. The ORCA program system. *WIREs Comput. Mol. Sci.* **2**, 73–78 (2012).
54. Frisch, M. J. et. al. Gaussian 09 Revision A.02 (Gaussian Inc., 2009).
55. Rahalkar, A. & Stanger, A. The Aroma Package, http://schulich.technion.ac.il/Amnon_Stanger.htm

Acknowledgements

This work was funded by NSF grant CHE-1800252 (C.A.G., J.R.L.), NSF grant DMR-1610226 (J.M., S.H.) and NIH grant 1R35GM126961 (D.A.M., R.D.B.). High-field EPR data were collected at the National High Magnetic Field Laboratory, which is supported by the NSF (DMR-1644779) and the State of Florida. NMR spectroscopy was collected at UC Berkeley's NMR facility in the College of Chemistry, which is supported in part by NIH grant S10OD024998. V.V. acknowledges a postdoctoral fellowship from Fonds Wetenschappelijk Onderzoek Vlaanderen (FWO, Flemish Science Foundation) and a V435018N FWO travel grant to UC Berkeley and C.A.G. thanks the NSF Graduate Research Fellowship Program for support. In addition, we thank L. A. Berben for the use of her gloveboxes, R. G. Bergman for insightful discussions and A. Stanger for advice on the Aroma program and $NICS_{zz}$ calculations. We also thank K. R. Meihaus for editorial assistance, N. S. Settineri for assistance with crystallography and A. B. Turkiewicz for keen observations.

Author contributions

Synthesis, crystallography and magnetic characterization were performed by C.A.G. High-frequency CW-EPR experiments were performed and analysed by J.M. and S.H. and D-Band EPR experiments were performed and analysed by D.A.M. and R.D.B. DFT calculations and computational analysis of aromaticity were performed by V.V. and L.F.C. The manuscript was written by C.A.G. and J.R.L. and edited by all authors.

Competing interests

The authors declare no competing interests.

Additional information

Extended data is available for this paper at https://doi.org/10.1038/s41557-021-00737-8.

Supplementary information The online version contains supplementary material available at https://doi.org/10.1038/s41557-021-00737-8.

Correspondence and requests for materials should be addressed to J.R.L.

Peer review information *Nature Chemistry* thanks Dongho Kim, Amnon Stanger, Dage Sundholm and Jishan Wu for their contribution to the peer review of this work.

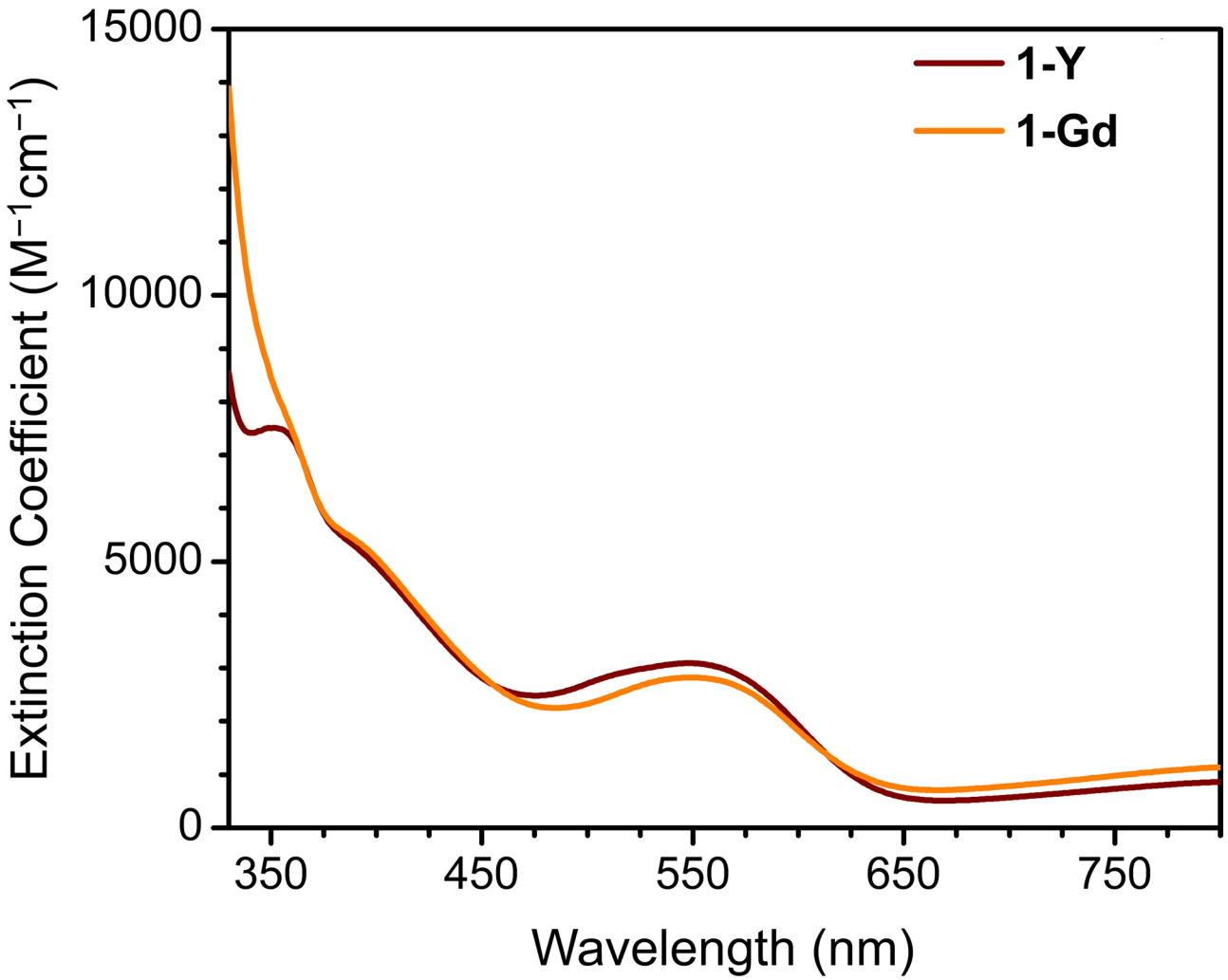

Extended Data Fig. 1 | UV-Vis-NIR spectra of [M2(BzN6-Mes)]⁻. Spectra of **1-Y** (maroon) and **1-Gd** (orange).

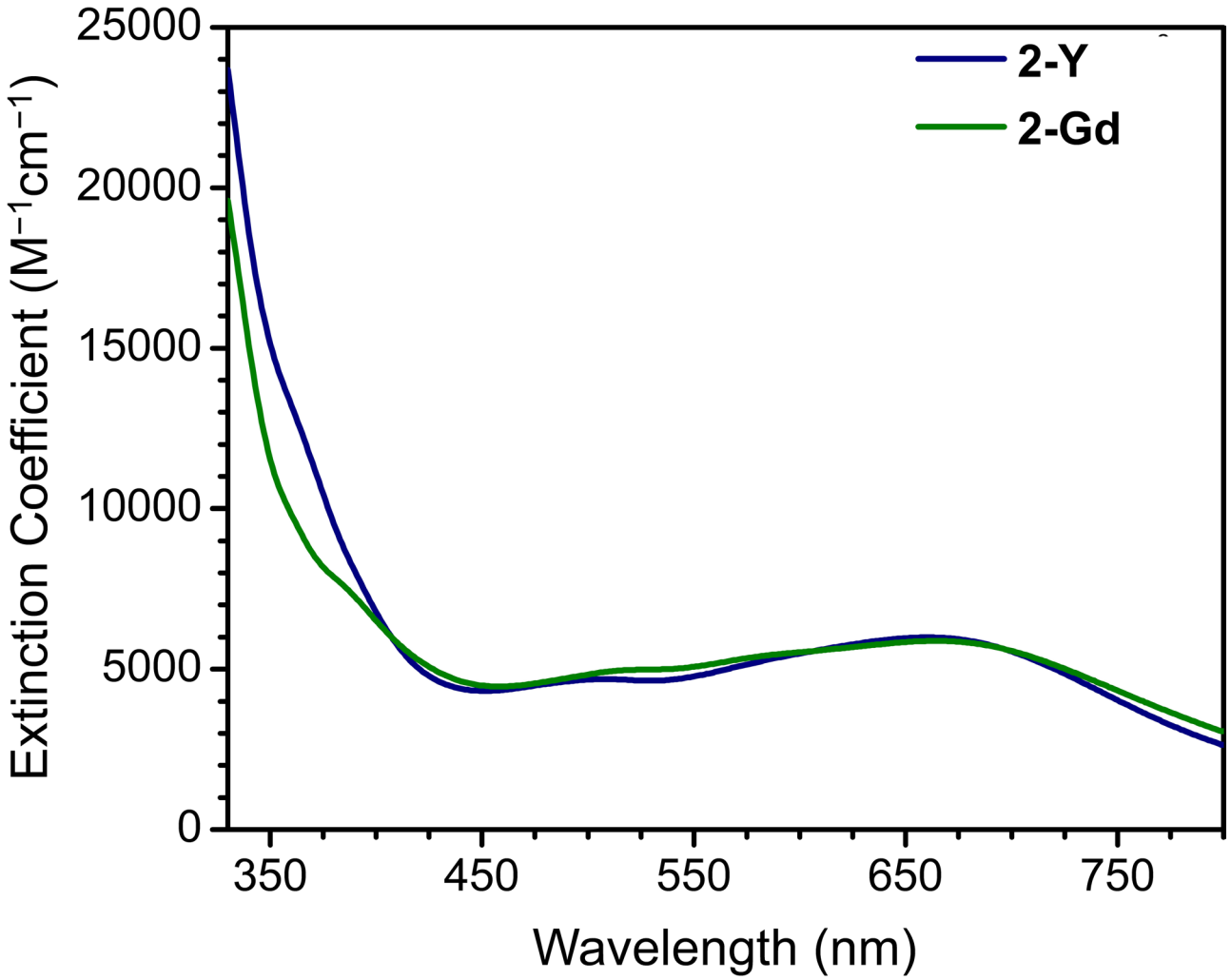

Extended Data Fig. 2 | UV-Vis-NIR spectra of $[M_2(BzN_6\text{-}Mes)]^{2-}$. Spectra of **2-Y** (blue) and **2-Gd** (green).

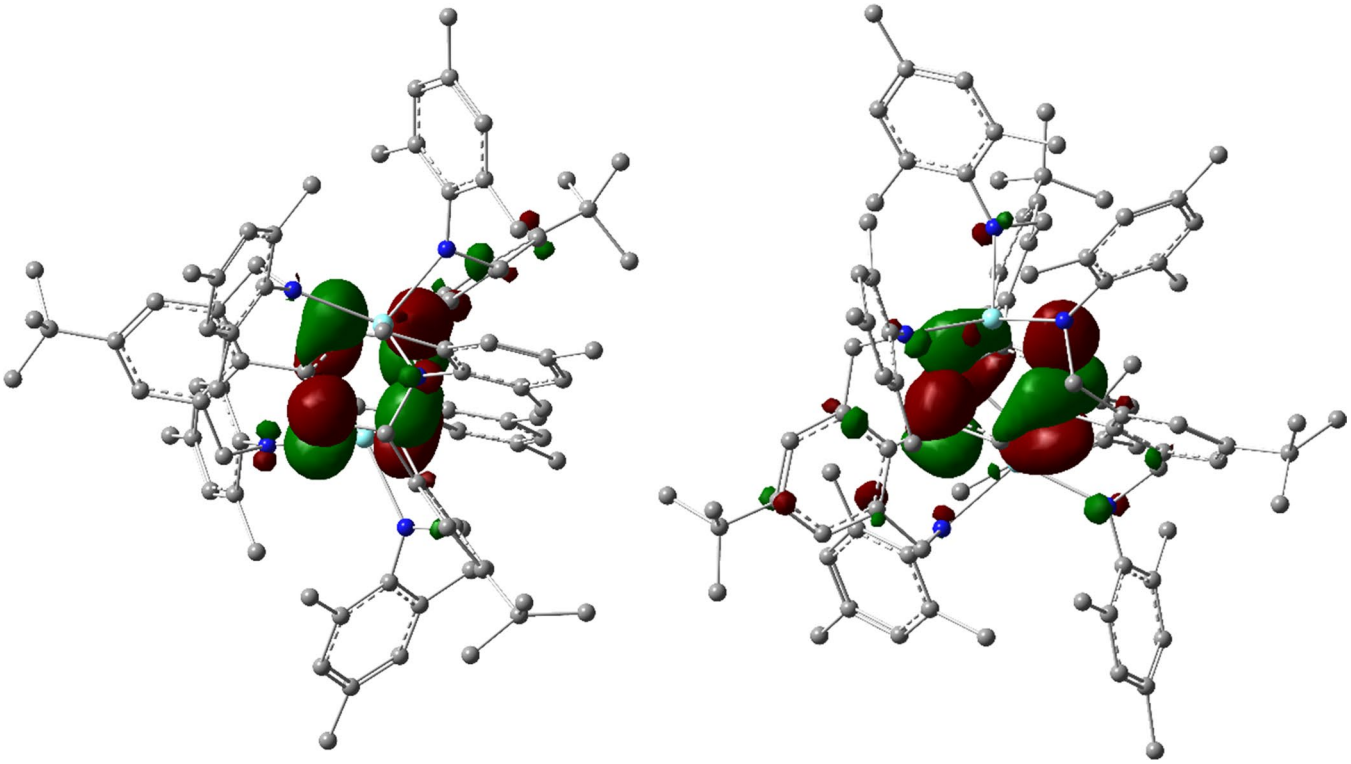

Extended Data Fig. 3 | Density functional theory calculations on 2-Y. The two singly-occupied molecular orbitals (SOMOs) obtained for **2-Y** by DFT calculations are localized on the central benzene ring of the BzN_6-Mes ligand.

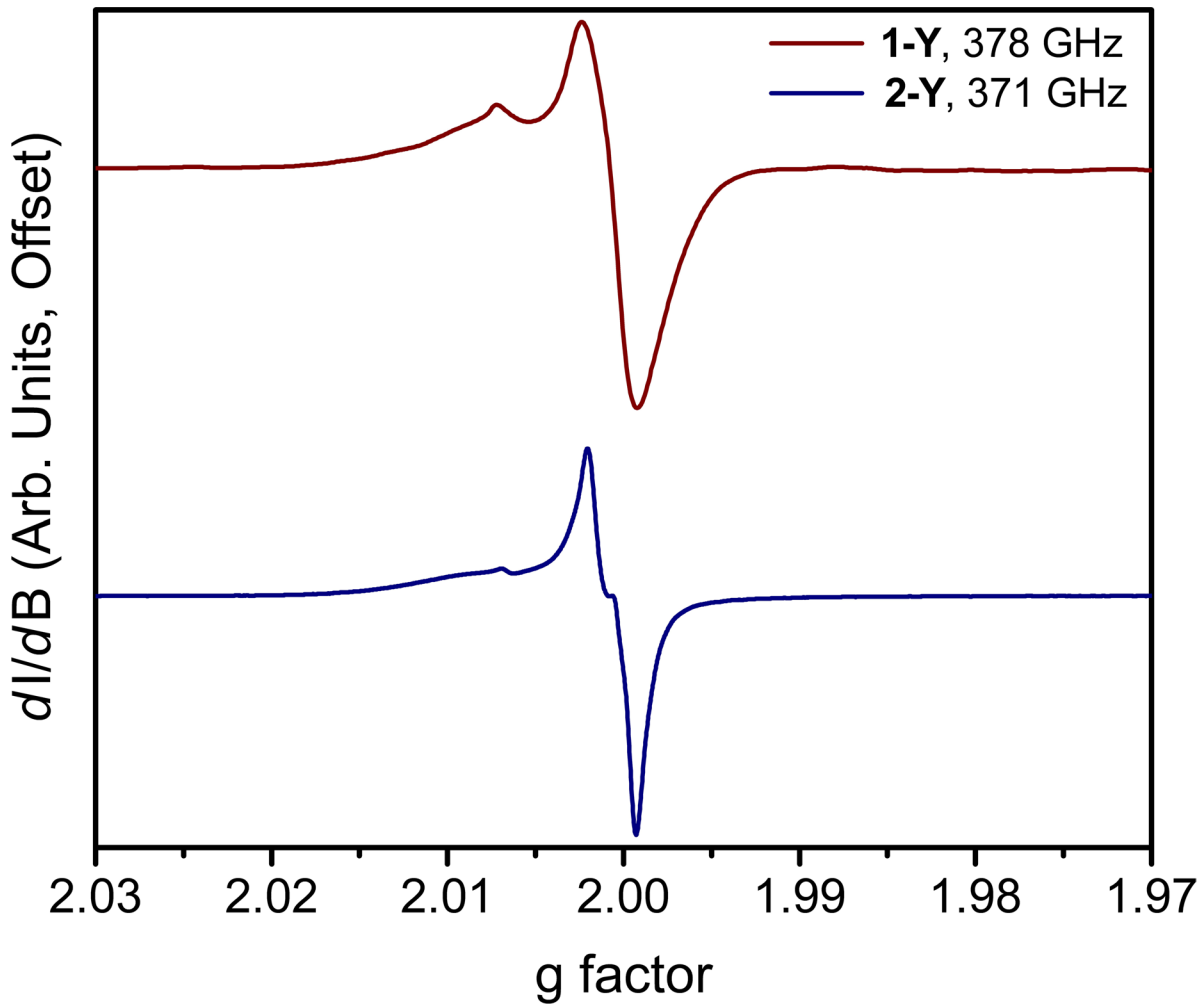

Extended Data Fig. 4 | CW-EPR spectra of **1-Y** (maroon) and **2-Y** (blue).

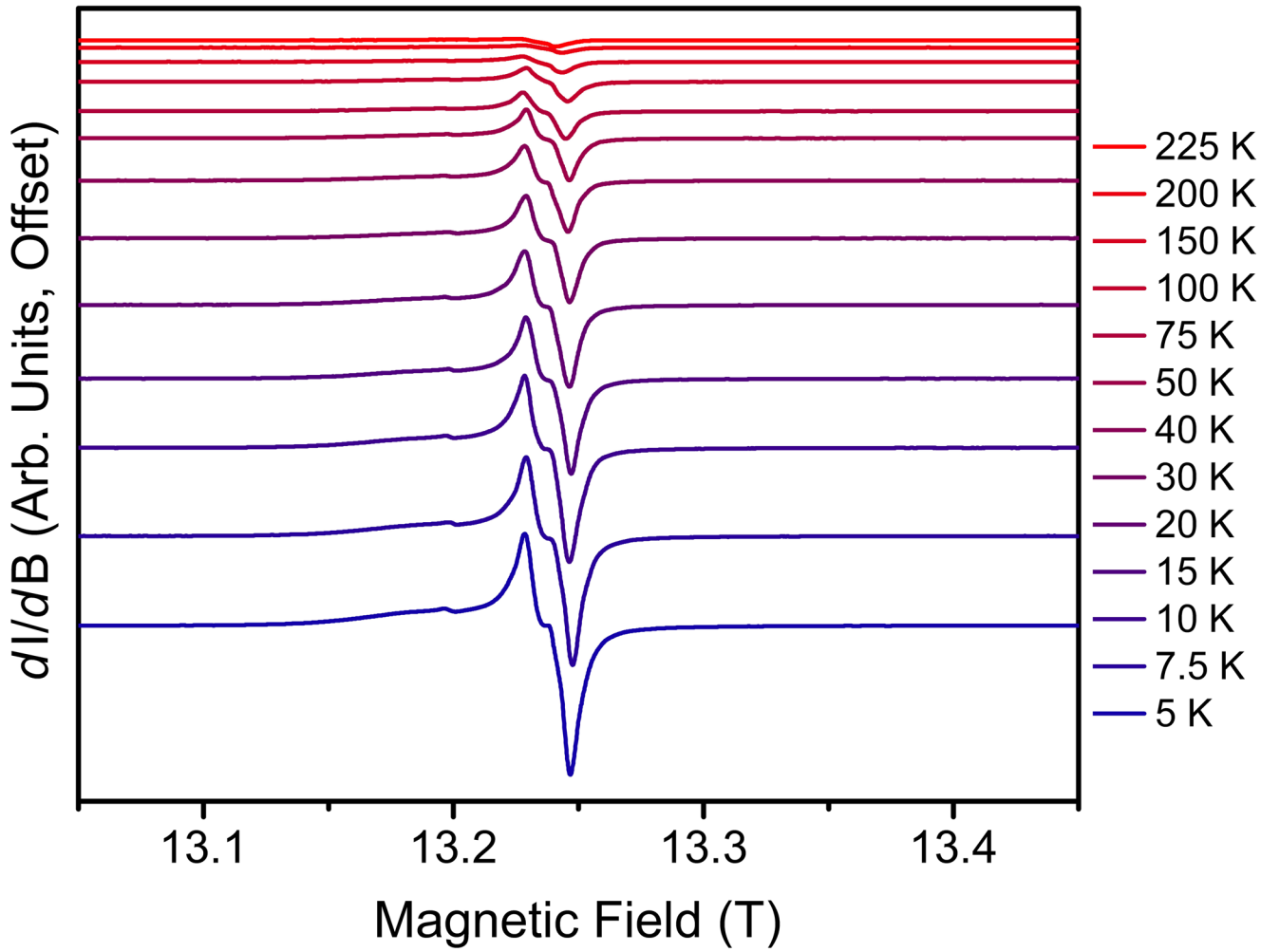

Extended Data Fig. 5 | CW-EPR spectra of **2-Y** from 5 to 225 K at 371 GHz.

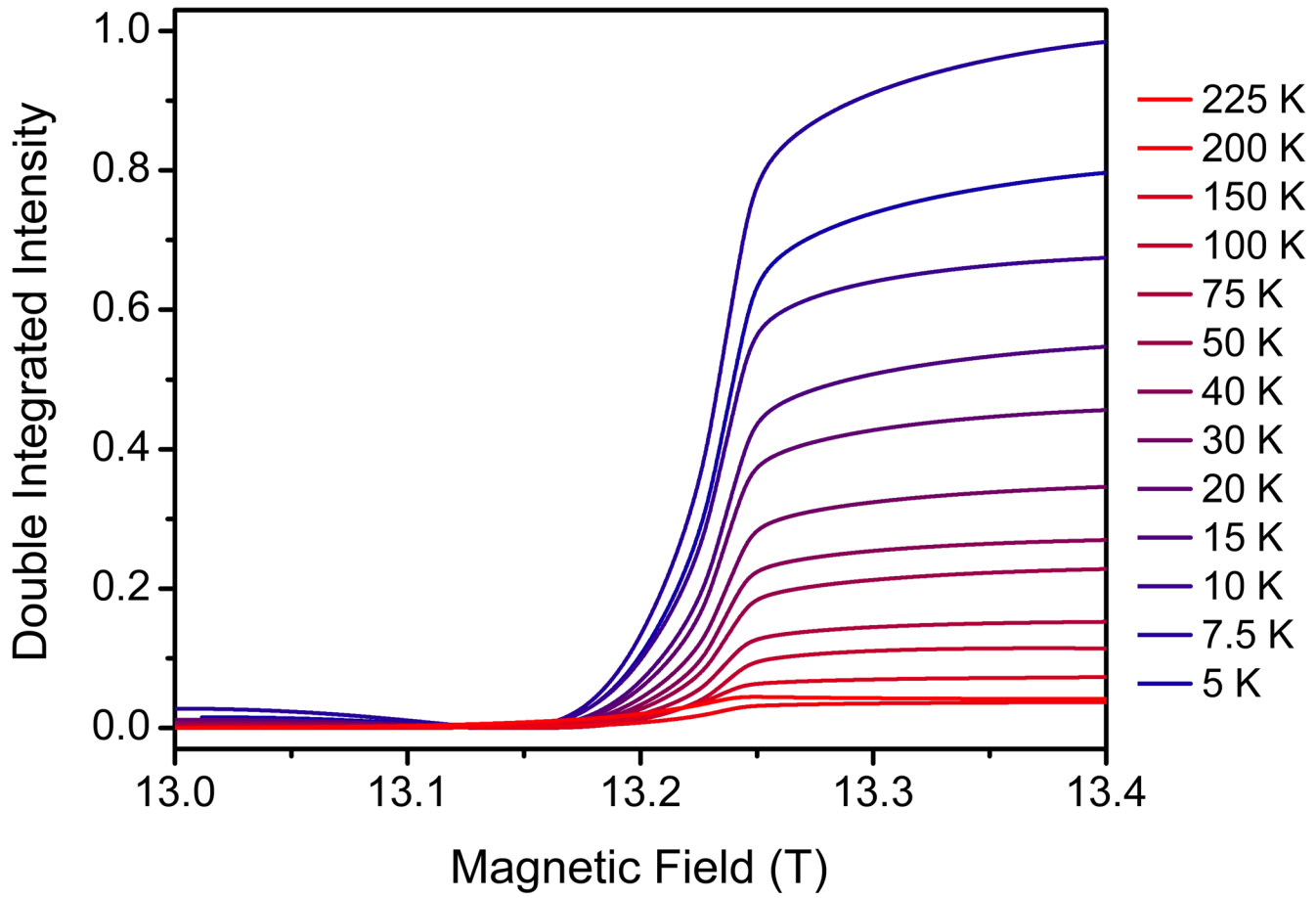

Extended Data Fig. 6 | Double integrated absorption of the EPR spectrum of **2-Y** from 5 to 225 K at 371 GHz.

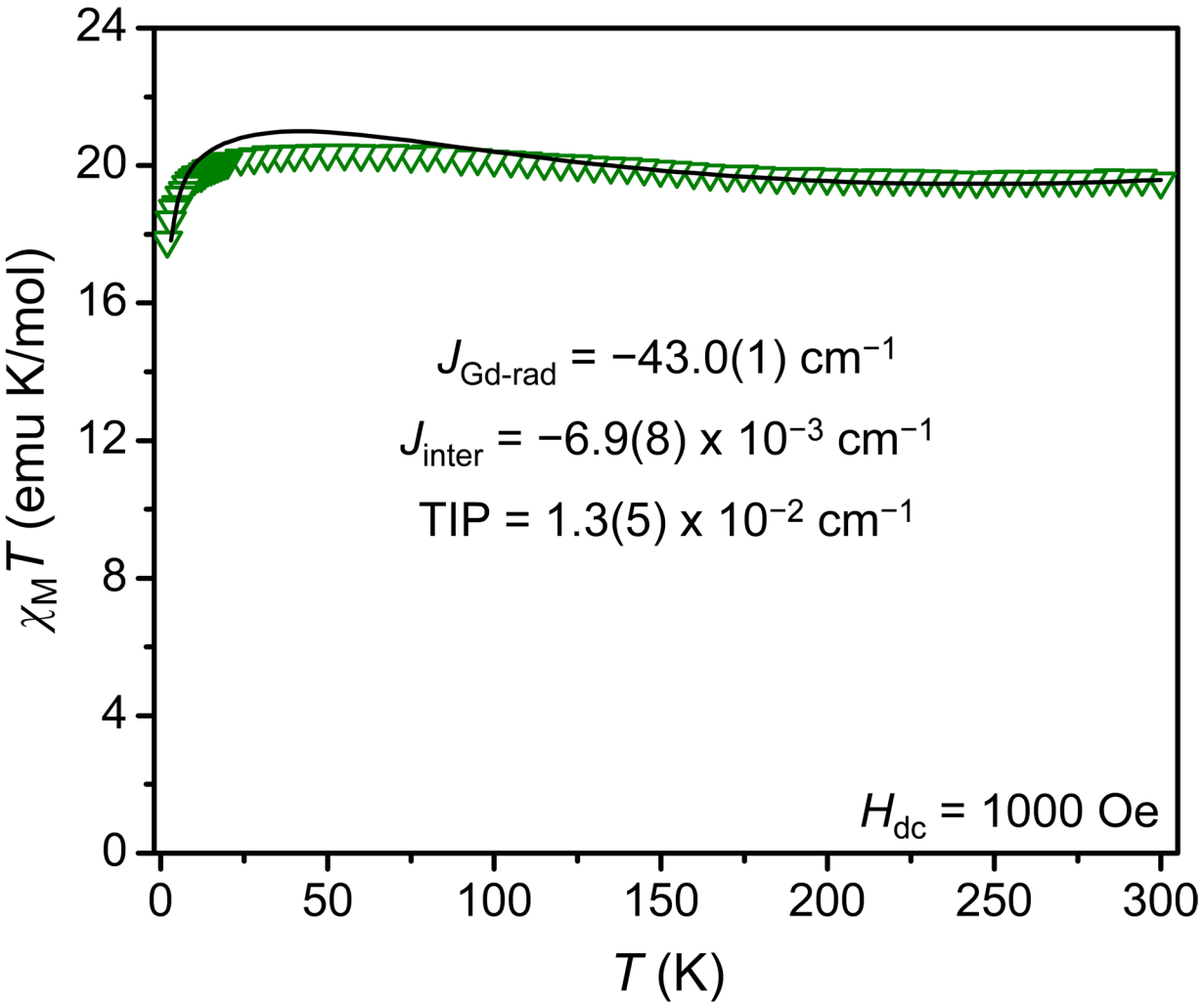

Extended Data Fig. 7 | Dc magnetic susceptibility measurement for 2-Gd under an applied dc magnetic field of 1000 Oe. The black line represents a fit to the data using the listed parameters.

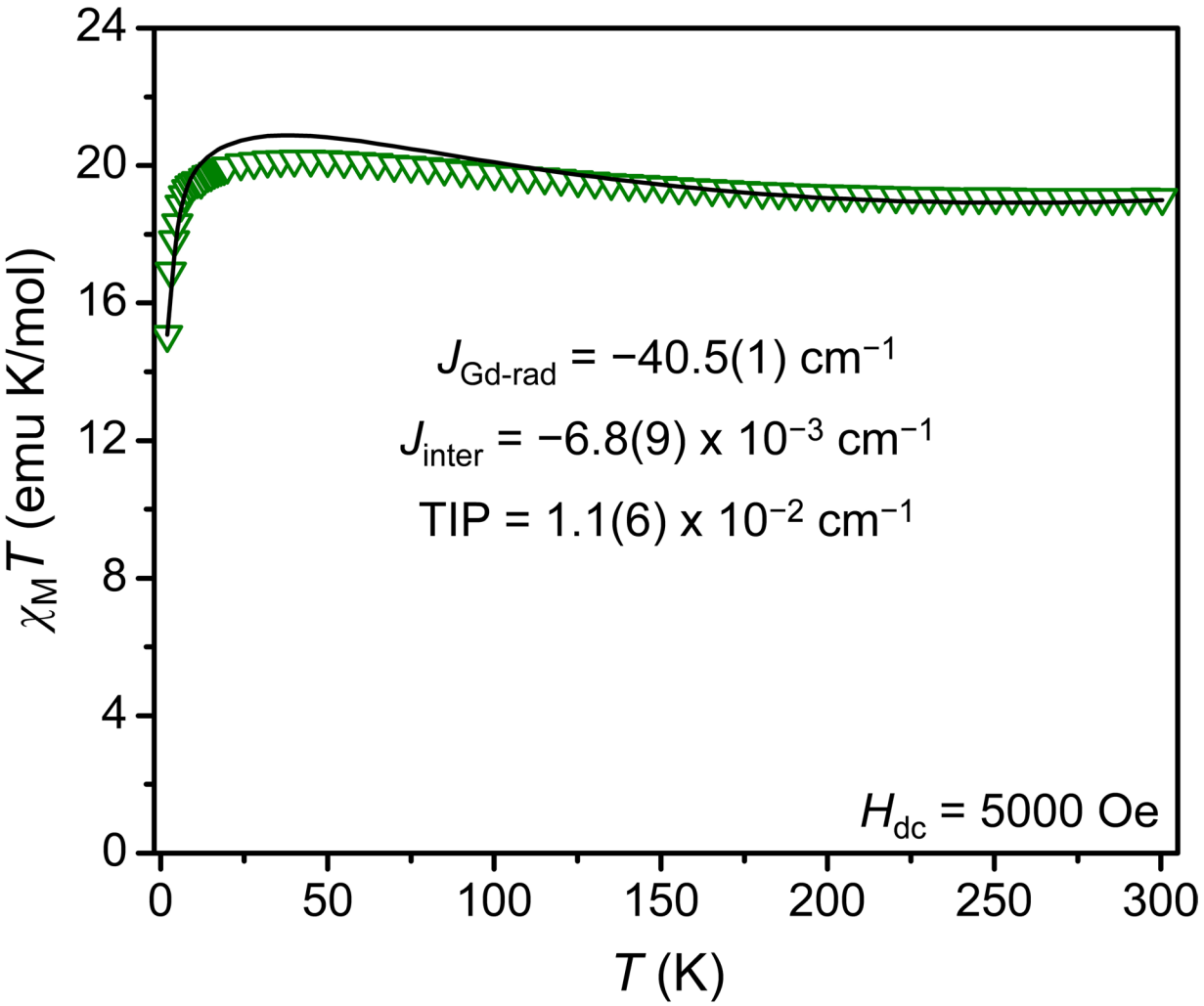

Extended Data Fig. 8 | Dc magnetic susceptibility measurement for 2-Gd under an applied dc magnetic field of 5000 Oe. The black line represents a fit to the data using the listed parameters.